JOURNAL OF GEOPHYSICAL RESEARCH, VOL. 113, A11209, doi:10.1029/2008JA013265, 2008

Large-scale dynamics of Saturn's magnetopause: Observations by Cassini

N. Achilleos,[1,2] C. S. Arridge,[2,3] C. Bertucci,[2,4] C. M. Jackman,[2] M. K. Dougherty,[2] K. K. Khurana,[5] and C. T. Russell[5]

Received 15 April 2008; revised 1 September 2008; accepted 8 September 2008; published 13 November 2008.

[1] The long-term statistical behavior of the large-scale structure of Saturn's magnetosphere has been investigated. Established statistical techniques for Jupiter have been applied to the kronian system, employing Cassini magnetometer data and a new empirical shape model of the magnetopause based on these data. The resulting distribution of standoff distance R_{MP} for Saturn, covering a time interval of ~400 days, is well-described by a "dual" or "bimodal" model—the sum of two normal distributions with different means at ~22 and ~27 planetary radii. We have made a comparison between the dual model's prediction for the probability distribution of solar wind dynamic pressure at Saturn with a sequence of observations from the Cassini Plasma Spectrometer (CAPS) instrument. Although the solar wind dynamic pressure observations are limited to a smaller time interval than the magnetometer data, we find that their overall range is in broad agreement with the that of the modeled pressures. However, the bimodal structure exhibited by the model is not apparent in the solar wind data for the corresponding range of dynamic pressures (~0.008 – 0.06 nPa), which suggests that other mechanisms at Saturn also influence the size distribution of the magnetopause. Considering internal processes at Saturn and their influence on magnetopause size, we conclude that the effect of internal mass loading and loss from the magnetospheric disk is plausibly able to explain the observed bimodal distribution in magnetopause standoff distance.

Citation: Achilleos, N., C. S. Arridge, C. Bertucci, C. M. Jackman, M. K. Dougherty, K. K. Khurana, and C. T. Russell (2008), Large-scale dynamics of Saturn's magnetopause: Observations by Cassini, *J. Geophys. Res.*, *113*, A11209, doi:10.1029/2008JA013265.

1. Introduction

[2] The solar wind continually flows around and past the magnetized planets of the Solar System. The solar wind in the vicinity of the giant planets flows at highly supermagnetosonic speeds, with Mach numbers typically exceeding ~8 [*Russell*, 1985, and references therein; *Slavin et al.*, 1985; *Achilleos et al.*, 2006]. Under these conditions, a bow shock forms upstream of the planet's magnetopause. The bow shock slows and diverts the solar wind about the forward magnetosphere which acts as an obstacle to the flow. In the subsolar magnetosheath the flow is most strongly slowed, compressed, and heated to the point of near-stagnation. The flow speed then increases as the width of the magnetosheath expands with increasing solar zenith angle. This fluid expansion results in the flow again becoming super-magnetosonic at solar zenith angles of ~40–50°, with a speed asymptotically approaching that of the upstream solar wind for locations downstream of the terminator region [*Spreiter et al.*, 1966; *Stahara et al.*, 1989].

[3] The size and shape of the magnetopause boundary at all magnetized planets yield important clues regarding the magnetosphere's internal structure. For example, the terrestrial magnetopause has a standoff distance R_{MP} (distance between planet center and subsolar nose of magnetopause) which scales as the $-1/6$ power of solar wind dynamic pressure (P_{SW}) in the upstream region: $R_{MP} \propto P_{SW}^{-1/\alpha}$ where the inverse index $\alpha = 6$ [e.g., *Shue et al.*, 1997]. This relation arises from the balance across the magnetopause between the magnetic pressure of a dipole-dominated magnetospheric field (which scales with radial distance R as R^{-6}) and the pressure exerted by the incident solar wind flow, which at the nose is approximately the upstream value P_{SW}. In addition, the location of the terrestrial magnetopause has a dependence on the direction of the upstream interplanetary magnetic field (IMF) [e.g., *Petrinec and Russell*, 1997].

[4] For a magnetosphere with significant internal sources of plasma, this size-pressure relation is characterized by a different scaling index; the case of Jupiter is an excellent

[1]Atmospheric Physics Laboratory, Center for Planetary Sciences, University College London, London, UK.
[2]Blackett Laboratory, Imperial College London, London, UK.
[3]Mullard Space Science Laboratory, Center for Planetary Sciences, University College London, Holmbury St Mary, London, UK.
[4]Now at Institute of Atronomy and Space Physics, Buenos Aires, Argentina.
[5]Institute of Geophysics and Planetary Physics, University of California–Los Angeles, Los Angeles, California, USA.

0148-0227/08/2008JA013265$09.00

illustration of this point. Jupiter's satellite Io (and its plasma torus) is the dominant source of plasma for the jovian magnetosphere, releasing $\sim$200–2500 kg s^{-1} into the planetary environment [e.g., *Delamere and Bagenal*, 2003; *Bagenal*, 1997; *Khurana and Kivelson*, 1993; *Hill*, 1980]. The magnetopause standoff distance for Jupiter lies most frequently near values of 63 and 92 R_J (1 R_J = jovian radius $\approx$ 71492 km), as determined by *Joy et al.* [2002, hereafter J02]. These large standoff distances, combined with Jupiter's rapid rotation (with period $\sim$10 hours), imply a large centripetal acceleration of the magnetospheric plasma as it diffuses from Io's orbit into the outer magnetosphere, maintained by the force of a highly radially "stretched" magnetic field, leading to an equatorially inflated or disk-like magnetosphere [e.g., *Acuña et al.*, 1983; *Walker and Russell*, 1995; *Hill et al.*, 1974; *Kivelson et al.*, 1997; *Kivelson and Southwood*, 2005].

[5] The power law index for the dependence of Jupiter's magnetopause standoff distance on dynamic pressure has been determined empirically, using the distributions of magnetopause crossings observed in situ by the Voyager and Pioneer spacecraft [*Slavin et al.*, 1985]. The resulting power law has α_J = 4.4, indicating a magnetosphere significantly more compressible than that of the Earth. *Huddleston et al.* [1998] considered additional crossings, over a wider range of latitudes, by the Ulysses and Galileo spacecraft. They derived a power law with α_J values between 4 and 5, in agreement with the results of *Slavin et al.* [1985]. Both of these studies thus confirmed that the jovian magnetosphere was highly compressible relative to the terrestrial system. They also demonstrated that Jupiter's magnetopause was flattened at the polar regions, by analyzing high-latitude crossings [*Huddleston et al.*, 1998], and identifying a relatively thin subsolar magnetosheath [*Slavin et al.*, 1985], consistent with a streamlined, disk-like magnetosphere.

[6] For the case of Saturn, *Slavin et al.* [1985] derived a magnetopause size-pressure relation with an Earth-like inverse index of α_S = 6.1. They commented, however, that their magnetopause shape models were not well constrained because of the paucity of effective (averaged groups of) crossings used in the fitting procedure. More recently, *Arridge et al.* [2006] (hereafter A06) were able to derive an updated empirical model for the magnetopause of Saturn, by analyzing the magnetometer data from the first seven orbits of the Cassini spacecraft. Discontinuous rotations in the magnetic field and/or changes in field strength and levels of field fluctuation were used to identify magnetopause crossings. The measured field strength inside the magnetopause (away from obvious boundary layer plasma) was used, as part of a Newtonian pressure balance condition, in order to estimate the solar wind dynamic pressure (the general interval studied did not have direct measurements by Cassini of dynamic pressure P_{SW} during solar wind excursions). Two of the particular strengths of the technique of A06 were: (1) it simultaneously fitted a magnetopause shape function as well as a pressure-size relation between R_{MP} and P_{SW}; and (2) it did not rely on direct measurements of P_{SW}. This aspect is advantageous for outer planet missions, which have not, as yet, involved spacecraft that are solely devoted to upstream monitoring of the solar wind conditions.

[7] Importantly, the power law index for the magnetopause size-pressure relation determined by A06 was α_S = 4.3 $\pm$ 0.4, significantly different from the terrestrial value and indicative of a Jupiter-like magnetospheric compressibility. Estimating the effects of hot plasma pressure in the force balance near the planetary equator, A06 concluded that these effects would change their α_S to a value closer to 5. They pointed out that a Jupiter-like value of α was consistent with the relative change observed by Cassini in the magnetopause standoff distance R_{MP}. For the orbits studied, this quantity varied by $\sim$30% of its average value ($\sim$25 R_S, 1 R_S = Saturn radius = 60330 km), similar to the relative change for the jovian system described by J02. It is important to note in this context the work in progress by S. Kanani et al. (Modelling the size and shape of Saturn's magnetopause using dynamic pressure balance, manuscript in preparation, 2008) aimed at updating the A06 model using accurate measurements of hot plasma pressure inside the magnetopause by Cassini. The values of the index α_S arising from these analyses are around 5.1, confirming the prediction by A06.

[8] We have mentioned the polar flattening of the jovian magnetopause. The study by *Slavin et al.* [1985] also discovered a magnetosheath at Saturn somewhat thinner than predicted for an axisymmetric magnetosphere, and the calculations of *Stahara et al.* [1989] explain these observations through a magnetopause obstacle with an elliptical cross section having a major (equatorial) axis $\sim$25% larger than its minor (polar) axis. More recent work presented by *Achilleos et al.* [2007] on high-latitude encounters with Saturn's magnetopause by Cassini confirms a flattening of this order. However, the restriction of these boundary crossings to the northern magnetosphere of Saturn and the lack of direct measurements of solar wind pressure make it difficult to disentangle the intrinsic flattening of the magnetopause (due to disk-like plasma distributions) from the "hinging" of the boundary produced by the non-orthogonal orientation of the planetary dipole with respect to the solar wind. The results of these ongoing studies are clearly of relevance to the current work, but a detailed study of the polar flattening of Saturn's magnetopause is beyond the scope of this paper.

[9] It was pointed out by J02 that the detailed probabilistic distribution of R_{MP} for a planet was also a diagnostic of the internal and external processes which influence magnetospheric size. This distribution could be built up from a knowledge of: (1) a scaleable shape model for the planetary magnetopause (J02 used polynomial 3-D fits to MHD simulations of Jupiter's magnetosphere); (2) the observed locations of magnetopause crossings; and (3) the relative time spent by the spacecraft in the regions inside and outside the magnetosphere.

[10] J02 examined observations of solar wind pressure measured by various spacecraft near Jupiter orbit. They concluded that the observed variability between the mean values in the distinct high-pressure and low-pressure states of the solar wind—a factor of 4.3—was not adequate to explain the difference ($\sim$30 R_J) between the two corresponding peaks at 63 R_J and 92 R_J in their modeled distribution of R_{MP} (for which a change in pressure by a factor of 7.8 was required). J02 concluded that there must also be changes in the contribution of internal plasma sources to the total pressure. These internal changes, com-

bined with the external variability in solar wind pressure, could plausibly account for the modeled difference in mean magnetopause size between Jupiter's two distinct (compressed and expanded) magnetospheric configurations.

[11] A possible explanation for the required significant variability of internal plasma sources at Jupiter may be the variable mass loading because of the Io source (the satellite and its plasma torus) operating at the same time as the loss of plasma mass via the Vasyliūnas cycle [*Vasyliūnas*, 1983]. Galileo observations of reconnection signatures in Jupiter's magnetotail field seem to support this picture and have been employed to provide an estimate of 2–3 days as the order of magnitude of the time scale associated with this cycle [*Russell et al.*, 2000; *Kronberg et al.*, 2005].

[12] In order to investigate the influence of the solar wind and mass loading on the size of Saturn's magnetosphere, we have applied the analysis techniques of J02 to the case of Saturn, employing Cassini magnetometer data and the empirical shape model for the magnetopause derived by A06. The resulting distribution of R_{MP} for Saturn is presented in section 3, where functional fits to the distribution are also reported. We find that a dual or bimodal fit–i.e., the sum of two normal distributions with different means–describes the behavior of magnetopause size at Saturn, in agreement with the corresponding result of J02 for Jupiter (more details are in Appendix A). We then compare our model's prediction for the probability distribution of the solar wind dynamic pressure at Saturn with a sequence of observations from the Cassini Plasma Spectrometer (CAPS) instrument (section 4). We also discuss in section 4 the differences between the mass loading processes at Jupiter and Saturn. We conclude that these internal processes are capable of affecting Saturn's magnetopause size dynamics, particularly bimodal distribution of standoff distance, and that their maximum effect is comparable to that of the solar wind variability.

2. Method

[13] For completeness, we describe the method used by J02 in order to derive statistical probability distributions of magnetopause size. In brief, the technique consists of the following steps:

[14] 1. Time Sampling of Data: Identify the magnetopause crossings in a set of spacecraft orbits. Sample the entire spacecraft trajectory using a chosen time step Δt and record at each sample time t_i whether the spacecraft was inside or outside the magnetosphere.

[15] 2. Modeling of Magnetopause Size: For every t_i, determine the standoff distance r_{MP} (t_i) of a magnetopause model surface which would pass precisely through the spatial location $\vec{x}_i$ of the spacecraft at that time. This will be a good approximation of the actual standoff distance R_{MP} only at the times of the magnetopause crossings. At all other times, it represents an estimate for the lower (upper) limit for the value of R_{MP} for samples found inside (outside) the magnetosphere.

[16] 3. Calculation of Probability Distribution of Magnetopause Size: Choose a set of bins in projected standoff distance, of width Δr_{MP} with centers at r^j_{MP} ($j = 1..N$ for N bins). Place each sample point into a bin according to its value of r_{MP} (t_i). Each of the N bins, corresponding to a particular value of standoff distance r^j_{MP}, will contain M_I samples inside the magnetosphere and M_O samples outside. The ratio $M_I/(M_I + M_O)$ is thus an estimation of the probability that the actual standoff distance exceeds the value r^j_{MP}. We denote this probability by P ($R_{MP} > r^j_{MP}$). This estimate will be more accurate for relatively small bin widths in conjunction with higher numbers of samples per bin. For a finite number of samples, these two properties are anti-correlated: there is a "trade-off" between them. In this case, an "optimum" bin width will generally exist which allows reasonably good probability estimates from an adequately large number of samples per bin, while at the same time allowing a good enough resolution of the typical length scales in r_{MP} over which this probability changes.

[17] For this study, the magnetopause model we have chosen is the empirical model by A06, described in the introduction. For the sake of completeness, we give here the functional form of the model magnetopause shape in terms of the radial distance r as a function of angular position θ:

$$r = R_{MP}(2/1 + \cos\theta)^{\kappa} \quad (1)$$

[18] The corresponding shape, originally used by *Shue et al.* [1997] for modeling the terrestrial magnetopause, is axisymmetric about the planet-Sun line (x axis). R_{MP} is the standoff distance (distance between planet center and the subsolar nose, where the x axis intersects the model shape); θ is the angle subtended at planet center between the x axis and the position vector of a point on the model surface; and κ is a "flaring parameter" whose value determines the rate at which the perpendicular distance $r \sin\theta$ changes as we move downstream to more negative values of $x(= r \cos\theta)$. Model shapes for the magnetopause which do not form a closed surface are characterized by $\kappa > 0.5$. A06 fitted the dependence of the parameters R_{MP} and κ on solar wind dynamic pressure P_{SW} into their model. For this study, we use the form of their model for which the scaling law between R_{MP} and P_{SW} is:

$$R_{MP} = a_1 (P_{SW})^{-1/\alpha} \quad (2)$$

[19] We also adopt the nominal relations and parameters reported by A06: $\kappa = 0.77–1.5\ P_{SW}$, $a_1 = 9.70$ and $\alpha = 4.3$, which are applicable when distance is measured in units of Saturn radii and pressure in units of nanoPascals (nPa). Note that κ and P_{SW} are anti-correlated in the fit of A06, contrary to the expectation that the higher Mach numbers in the outer solar system should produce more blunt magnetopause shapes. However, this anti-correlation is relatively weak (the coefficient of 1.5 accompanying P_{SW} has a large relative error of 20%, and for the typical solar wind pressures at Saturn changes κ by <10%); and the longer dayside-to-tail transport time for magnetic flux at Saturn may also affect the flaring in an unexpected manner (discussed by A06). The conclusions of our study and the results of our fitting (section 3, Appendix A) are not significantly affected if we use a form of the Arridge model with self-similar scaling, fixing κ at a constant value of $\kappa = 0.74$, corresponding to a typical value of $P_{SW} = 0.02$ nPa.

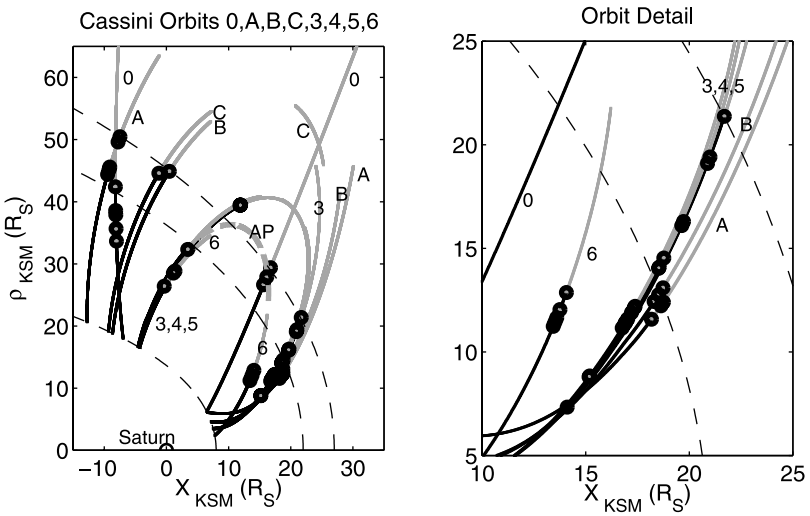

Figure 1. Sampled trajectory of Cassini during Revs 0 through 6, in the cylindrical KSM system. Magnetopause crossings are shown as open circles. Orbit segments inside (outside) the magnetosphere are colored black (gray). Orbits are labeled with their "Rev" identifier (see text). The label "AP" and dashed gray segment denotes the Rev 5/6 apoapsis. The thin dashed curves are versions of the A06 magnetopause model with standoff distances at 8, 22, and 27 R_S.

[20] In order to obtain a baseline data set of projected standoff distances $r_{MP}(t_i)$, we sampled the first seven orbits of the Cassini spacecraft. In mission parlance, these are known as Revolutions 0, A, B, C, 3, 4 and 5. These particular orbits were used in the original derivation of the A06 empirical magnetopause model and are therefore appropriate for the present analysis. In order to check the persistence of the distribution in standoff distance, an extended data set of r_{MP} (t_i) values was also computed, using the first 16 orbits of the spacecraft (Revolutions 0 through 14). Taken as a whole, these orbits span a time interval of ~430 days (from 1 July 2004 to 3 September 2005). We sampled the orbits using a time interval of 5 minutes and, following J02, we checked larger sampling times (10 minutes, 20 minutes) to ensure that our conclusions were not affected. We found that the baseline and extended distributions derived from the data were in agreement. This result suggests that the A06 model remains a good approximation to magnetopause shape for orbits beyond those used in its original construction (see section 3 for details).

[21] We repeated the analyses described herein with the incorporation of the Voyager magnetopause crossings into the much larger Cassini data set. Our distribution of standoff distances was not significantly affected. However, the Cassini crossings do not exceed ~30 R_S in standoff distance, while the Voyager 2 crossings reach ~35–40 R_S. This difference is consistent with the interpretation that the planet was immersed in Jupiter's magnetotail during the V2 flyby and subject to unusually low upstream dynamic pressure [e.g., *Scarf et al.*, 1981; *Behannon et al.*, 1983].

[22] The coordinate system used to describe orbital and model geometries is the cylindrical form of the Kronocentric Solar Magnetospheric (KSM) system, with origin at Saturn, x_{KSM} axis pointing in the direction of the Sun, and ρ_{KSM} denoting the perpendicular distance from the x_{KSM} axis.

3. Magnetopause Size Distributions

[23] Figures 1 and 2 show the Cassini spacecraft trajectory in the cylindrical KSM system for the time interval

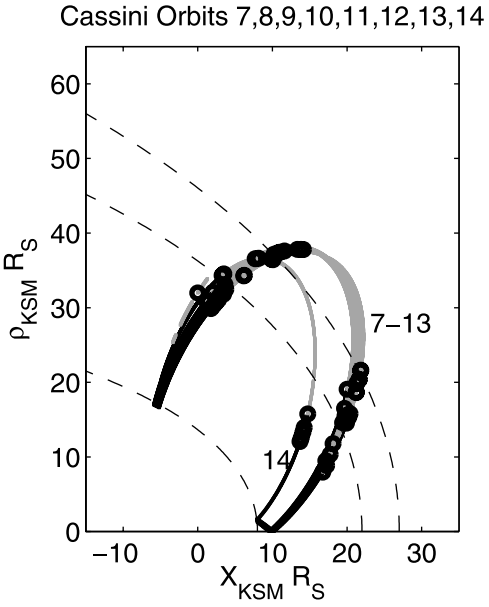

Figure 2. Sampled trajectory of Cassini during Revs 7 through 14, in the cylindrical KSM system. Magnetopause crossings are shown as open circles. Orbit segments inside (outside) the magnetosphere are colored black (gray). Orbits are labeled with their "Rev" identifier (see text). The thin dashed curves are versions of the A06 magnetopause model with standoff distances at 8, 22, and 27 R_S.

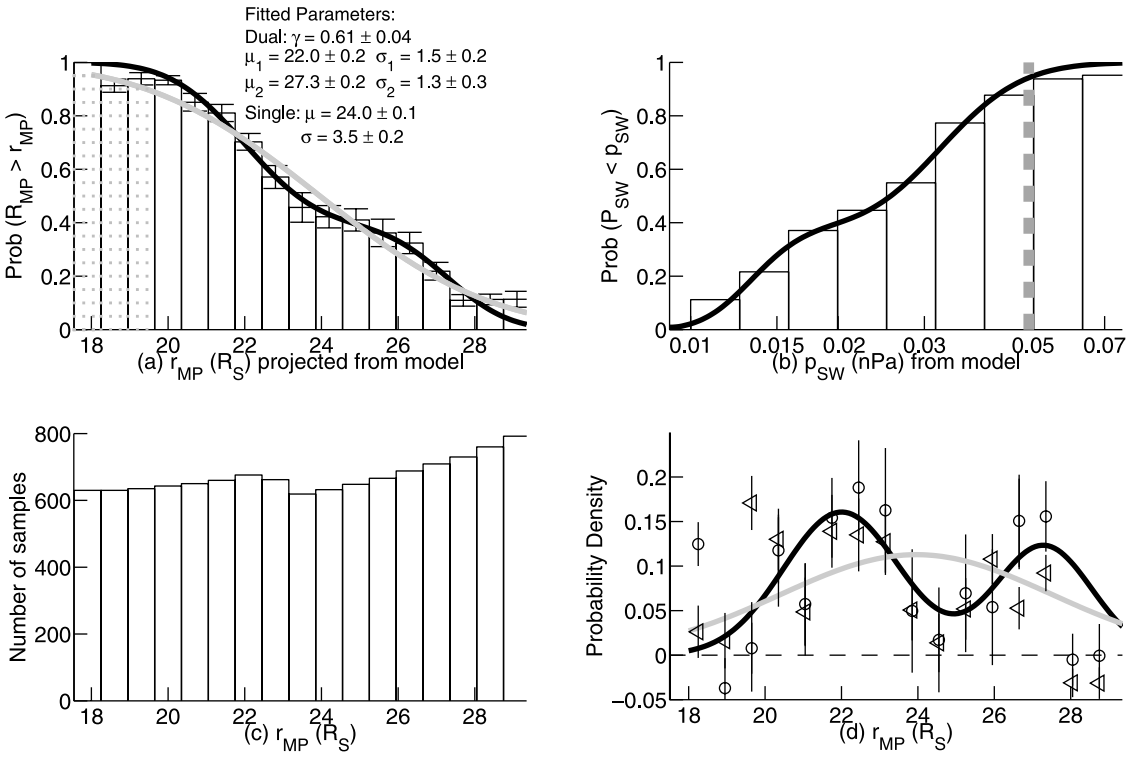

Figure 3. (a) Cumulative probability distribution for standoff distance R_{MP}, with best baseline fits shown for dual and single normal populations (Revs 0 through 5). Bins have width 0.7 R_S—those with square "hatching" are not used for fitting (see text and Figure 4). (b) Probability as a function of modeled solar wind pressure. The dashed gray line shows p_{SW} corresponding to r_{MP} = 20 R_S. (c) Variation in number of samples per bin for the baseline fit. (d) Solid curves are modeled probability density functions (PDFs) corresponding to the baseline fits in (a). The observed PDF for the baseline data set (Revs 0 through 5) is shown as open circles with error bars. Triangles represent the similar observed PDF when Revs 0 through 14 are used in the analysis.

under study. The magnetopause crossings, as well as the segments of the orbits located inside and outside the magnetosphere, are identified. The magnetometer data set was used, as in A06, to identify the crossings of the boundary. One major "gap" in the orbital coverage arises from the "no command" period associated with the Huygens probe mission during Day of Year (DOY) 7 to 15 January 2005. We have also omitted the Rev 5/6 apoapsis (2005, DOY 94-102 (4–12 April)), to avoid biased sampling in the region between the two models with R_{MP} = ~22 and ~27 R_S (as described in the following paragraph).

[24] This region (~22 R_S < R_{MP} < ~27 R_S) is important, because these two model surfaces are where most orbits (Rev 6 is the exception) show transitions between segments predominantly inside and outside the magnetosphere. Furthermore, the boundaries of this "transition" region extend over a wide range in planetary local time (pre-dawn to pre-noon), indicating a global transition from magnetosphere to magnetosheath in this region, rather than the magnetopause moving more freely at particular local times. J02 pointed out that orbits with apoapses in such a region, under a scheme of regular time sampling, would add unrealistically large numbers of samples to the data set that reflect magnetospheric conditions during the relatively low-velocity apoapsis intervals. We intend to explore this aspect in a future study, where a sampling time dependent on the rate of change of $r_{MP}(t_i)$ will be investigated. For present purposes, we have omitted the apoapsis in the transition region, whose inclusion did not significantly affect the fitting results of section 3.

[25] We computed the cumulative probability distribution $P(R_{MP} > r_{MP})$ for projected standoff distances r_{MP} between 18 and 30 R_S (encompassing the transition region) and various bin sizes. Figure 3a shows the resulting baseline distribution (Revs 0-5) for a bin size Δr_{MP} = 0.7 R_S (this bin size produced the most statistically significant model fits to the data as reported in Appendix A). The error bars shown for the probability in each bin were calculated according to the Monte Carlo techniques of J02 and A06: 40 random "subsamples", each comprising 20% of the bin's total population, were used to calculate a probability, with the resulting standard deviation used as a measure of the uncertainty. Following J02, we performed non-linear least squares fits of the cumulative probability distribution, using the following functional form corresponding to the weighted sum, according to the factor γ, of two normally-distributed populations:

$$P_C(r_{MP}) = \int_{r_{MP}}^{\infty} [\gamma P_{DN}(r;\mu_1,\sigma_1) + (1-\gamma)P_{DN}(r;\mu_2,\mu_2)]dr$$
$$P_{DN}(r;\mu,\sigma) = \left(1/\sigma\sqrt{2\pi}\right)\exp\left(-(r-\mu)^2/2\sigma^2\right) \quad (3)$$

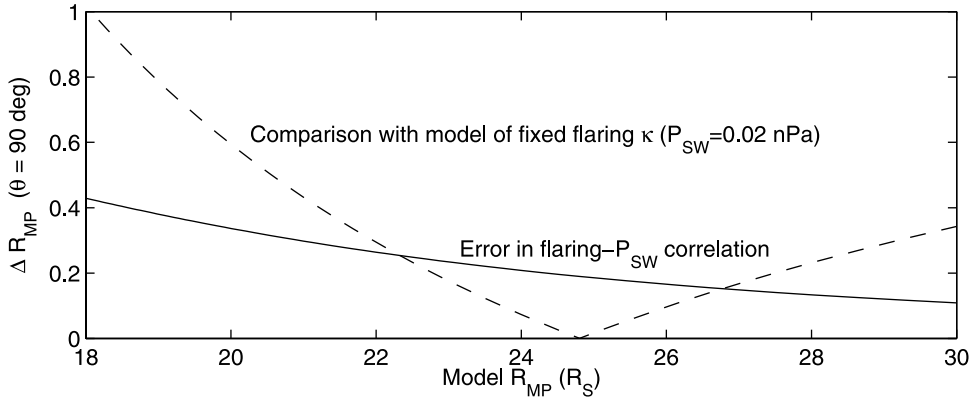

Figure 4. The curves show the difference (uncertainty) which arises when the magnetopause standoff distance R_{MP} is computed from points on the terminator ($\theta = 90°$) of different geometrical models. The solid curve shows the variation due to the uncertainty in the correlation between P_{SW} and κ of the A06 model (see also equation 1). The dashed curve shows the variation between two versions of the A06 model: (1) with this correlation included and (2) with κ set to a constant value of 0.74, corresponding to $P_{SW} = 0.02$ nPa (see text). For $R_{MP} <\sim 20\ R_S$ the mean uncertainty becomes comparable to typical values of bin width ($\sim$0.5 R_S) used in this study.

[26] Following J02, we computed two types of least-squares fit: a bimodal or dual fit using the full form of equation (3); and a single fit for which γ was fixed at unity, and the data were fitted with a single normal distribution. The fit itself was computed using the Matlab optimization toolkit, which uses an interior-reflective Newton method [*Coleman and Li*, 1996]. Uncertainties in the model parameters were calculated by repeating the fit for the 40 random subsamples described above and taking the standard deviation in each parameter. For calculations of the fitted parameters, we only considered data from bin centers $r_{MP} \geq 20\ R_S$. This was because, for $r_{MP} < 20\ R_S$, the uncertainty in the flaring of the A06 model implied that the quantity r_{MP} could not be estimated with an accuracy better than typical bin sizes. Figure 4 shows the estimated uncertainty in calculating the standoff distance associated with a point which lies on the A06 magnetopause terminator ($\theta = 90°$). Using equation 1 with $\theta = 90°$, the nominal standoff distance projected from a terminator point at radial distance r is $R_m = r/2^{\kappa}$. The solid curve in Figure 4 shows the uncertainty δR_m which arises from simply propagating the uncertainty in κ given by the fitting results of A06. The dashed curve shows an alternative estimate of δR_m which was calculated according to the formula $\delta R_m = |r/2^{\kappa} - r/2^{\kappa_o}|$ with $\kappa_o = 0.74$ (corresponding to $P_{SW} = 0.02$ nPa). This formula describes the difference between the nominal value of R_m (taking into account the pressure dependence of κ) and the value associated with a fixed flaring parameter κ_o (evaluated at $P_{SW} = 0.02$ nPa, the average pressure value). We note that a fixed flaring parameter corresponds to the case where the shape of the magnetopause scales in a self-similar manner (i.e., the radial distance of all points on the boundary is dilated by the same constant factor).

[27] It is visually apparent from Figures 3a and 3d that the dual model provides a fit in better agreement with the data; however we will discuss in Appendix A the statistical significance of this improvement over the single fit. The best-fitting dual model has mean values for its two components of $\mu_1 \sim 22\ R_S$ and $\mu_2 \sim 27\ R_S$, reflecting the pattern of the spacecraft orbits seen in Figure 1. The standard deviations for the two components are in the range $\sim$1–2 R_S and have larger associated relative uncertainties than the means. The fitted value of γ indicates that, for the orbits studied, the system spends 60% of the time in the more compressed configuration. This aspect reasonably agrees with the corresponding jovian model of J02, which had the two components at equal weighting.

[28] Figure 3b shows the cumulative probability distribution (for Revs 0–5) as a function of the modeled solar wind pressure p_{SW}, i.e., the probability that the actual solar wind pressure P_{SW} is less than the value of the abscissa (plotted on a log scale). Two local regions of maximum slope in the dual fit are seen at values of $p_{SW} \sim 0.012$ and 0.03 nPa, corresponding to the regions near $r_{MP} \sim 22$ and 27 R_S in Figure 3a. Figure 3c shows the number of samples in each of the bins associated with the projected standoff distance r_{MP}. The variation in this quantity between adjacent bins is reasonably smooth (<6% relative difference) and free of the large "spikes" which would be associated with a data set biased by too many samples near one particular projected standoff distance. As a fraction of the distance between the "peaks" of the dual distribution ($\Delta\mu_S = 5\ R_S = 27–22\ R_S$), this bin width is equal to $\sim$0.14 $\Delta\mu$. J02 used a similar relative bin width for their study of Jupiter's magnetopause. It is important to note in this context that the standard deviations for the jovian magnetopause distribution were $\sigma_J \sim 5\ R_J$, which is equivalent to $\sim$0.17 $\Delta\mu_J$, while, at Saturn, we see from Figure 3 that $\sigma_S \sim 1.5\ R_S \sim 0.3\ \Delta\mu_S$, a larger fraction.

[29] In Figure 3d, we have calculated the probability density function (PDF) for the standoff distance. The solid lines show the PDF associated with the baseline model fits (dual and single). The symbols denote the PDFs derived from the data by taking finite-difference derivatives of the cumulative probability values. The similar data-based PDFs for the baseline (Revs 0–5) and extended (Revs 0–14) data sets are shown as circular and triangular symbols respectively. Repeating the dual model fit for the extended data set

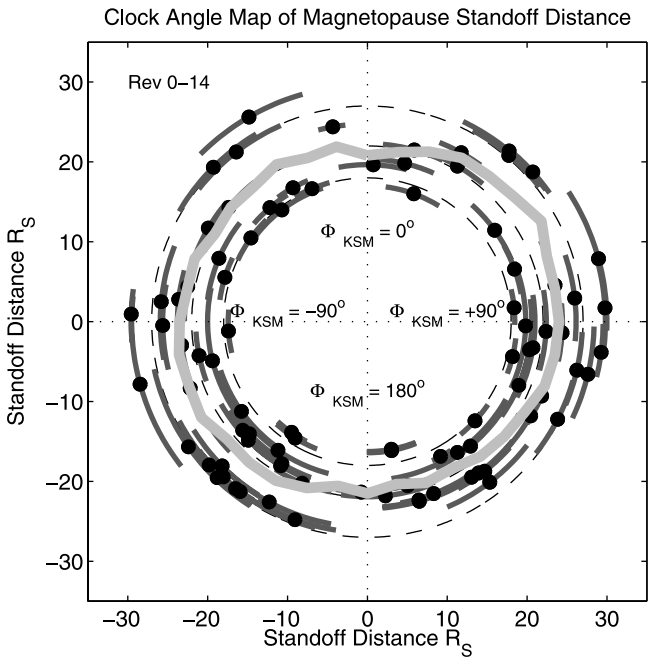

Figure 5. Polar map of magnetosheath field orientation (azimuthal position of circular dots on the plot) versus magnetopause standoff distance (radial distance from origin) for Revs 0–14. Steady field orientations within 1 hour of magnetopause crossings were chosen (see text) and the gray arcs represent the standard deviation in KSM clock angle Φ_{KSM} (see text). The thick, light gray line shows average clock angle computed over 45-degree windows, displaced by 10° steps to cover the full plane. Φ_{KSM} = 90° is the positive *Y* axis in KSM coordinates, and Φ_{KSM} = 0° is the positive *Z* axis (projection of the planetary dipole onto the plane of the graph) in the same system.

yielded parameters similar to the baseline fit, namely: (μ_1 = 2.1 ± 0.2, μ_2 = 26.9 ± 0.2, σ_1 = 2.0 ± 0.4, σ_2 = 1.0 ± 0.3, γ = 0.77 ± 0.04). These agree with the baseline fit results to within approximately twice the error or less. Adopting either the baseline or extended model does not alter our conclusions in this paper. In the following sections, we have decided to refer to the baseline model parameters. We note that the ''valley'' between the two peaks in the R_{MP} distribution for Saturn is characterized by a probability densities ∼5% per unit distance (planetary radius), somewhat higher than the near-zero value for the more well-separated peaks of the jovian system (J02).

[30] The effect of the upstream magnetic field may also influence magnetopause structure, particularly if it promotes magnetic reconnection and the consequent ''eroding'' of the magnetopause boundary. A06 discussed the possible influence of reconnection on the size and shape of Saturn's magnetopause. Auroral and in situ studies at Saturn seem to indicate that magnetic reconnection does occur [e.g., *Badman et al.*, 2005; *McAndrews et al.*, 2008]. However, the effect of the IMF orientation on Saturn's magnetospheric size and dynamics seems to be secondary to that of solar wind pressure [e.g., *Crary et al.*, 2005] and a quantitative description based on observations has yet to be determined.

[31] While such an exercise is beyond the scope of this paper, we were able to find magnetosheath intervals within 1 hour of 89 of our magnetopause crossings (from Revs 0–14) for which the field orientation was steady over 10 minutes to 1 hour. By ''steady'', we mean that the KSM clock angle defined by $\Phi_{KSM} = \tan^{-1}(B_Y/B_Z)$ exhibited root-mean-square fluctuations of less than 20° (the XZ plane in KSM coordinates contains the planetary dipole direction, with X pointing from Saturn's center toward the Sun and Y completing the orthogonal system). For most of these intervals, one-minute averaged magnetometer data showed compressional fluctuations characteristic of magnetosheath plasma, with large relative fluctuations in field strength coincident with a much more stable field orientation.

[32] In Figure 5, we plot Φ_{KSM} on an azimuthal scale, accompanied on the radial scale by the standoff distances of each corresponding magnetopause crossing. Thus each point in the plot represents magnetospheric size through its distance from the origin, and KSM clock angle through its azimuthal angle. We see a large range in standoff distance over all clock angles, although the sampling is poorer near Φ_{KSM} = 0° and 180° (an effect of the spacecraft being situated more frequently outside the heliospheric current sheet). The thick, light gray curve shows the average standoff distance calculated over a moving 45° window in clock angle. There is a small modulation in this quantity, with the average standoff distance ∼2 R_S smaller for magnetosheath fields near Φ_{KSM} = 0° and 180° (i.e., northward and southward) compared to Φ_{KSM} = ±90°. This behavior is generally consistent with the solar wind structure in the Cassini era described by *Jackman et al.* [2004], where heliospheric current sheet crossings are embedded in compression regions, and lower average solar wind pressures (roughly indicated by IMF strength) prevail outside the current sheet, where the field is most closely aligned with a Parker spiral configuration at Saturn (near Φ_{KSM} ∼ ±90°). There is no evidence from this representation of the

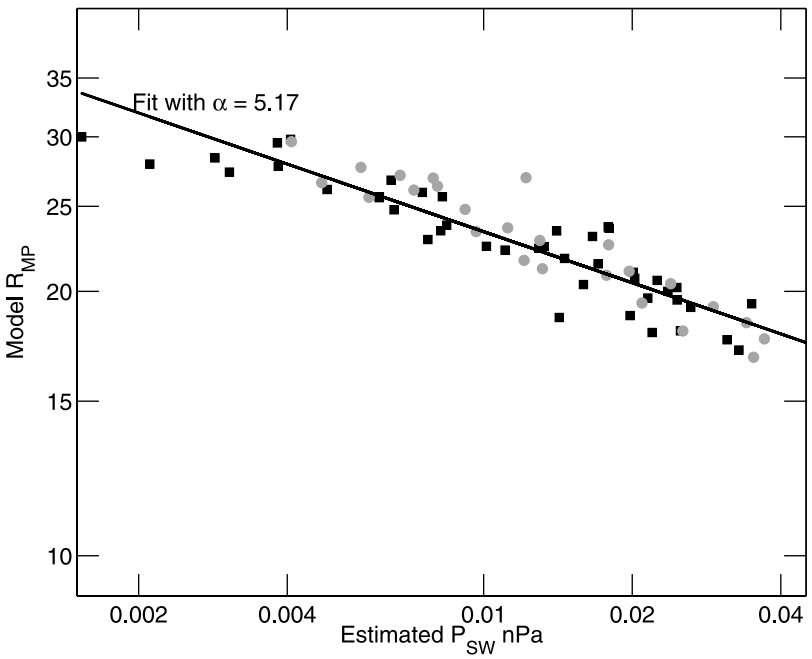

Figure 6. Magnetopause standoff distance versus solar wind dynamic pressure for the 26 crossings used in A06 (circles) and the 44 additional crossings analyzed in this study (squares). Standoff distance was obtained by using the geometry of the A06 model coincident with each crossing, and dynamic pressure was estimated as in A06, using measured interior magnetic pressure and assuming a zero-beta magnetospheric plasma confined by a magnetopause in pressure balance (see text for more detail). The best-fitting power law is shown (solid line).

data that northward IMF directions which favor magnetic dayside reconnection ($\Phi_{KSM} \sim 0°$) are associated with significantly smaller standoff distances than all other field orientations.

4. Physical Origin of Variability in Magnetopause Size

[33] In the context of the probability distribution of magnetopause standoff distance R_{MP} that we have derived from the Cassini data set, the statistical tests used in Appendix A indicate that the dual model, which superposes two normal populations in R_{MP}, provides the better fit. At bin sizes $<\sim 0.9\ R_S$, the dual model can generally be accepted at levels of significance $>\sim 10\%$, compared to a few percent at most for the single model. Given that the long-term behavior of the magnetopause size, measured by R_{MP}, is indicated to be bimodal, it is natural to seek a physical explanation for this behavior.

[34] Before we discuss possible physical causes, it is important to point out that the bimodal distribution in the magnetopause standoff distance is not dependent on the precise value for the magnetospheric compressibility index α_S (section 1). This index does however determine the values of solar wind pressure corresponding to the most common standoff distances. In the following sections, we continue using the power law of the A06 model, for which $\alpha_S = 4.3$ and the standoff distances at the "peaks" of the distribution (22 and 27 R_S) map to solar wind pressures of ~ 0.03 and 0.012 nPa. Changing α_S to larger values decreases the pressure value for a fixed R_{MP}.

[35] As a means of investigating the range of plausible values for α_S, we used measurements of interior magnetic pressure for 44 crossings on Revs 7–14 (following A06, we chose steady intervals of magnetic field strength of duration 20 minutes–1 hour, within 1 hour from the crossing, and showing quadrature-summed r.m.s. fluctuations in the field components <10% of the mean field strength). Adding these to the original data from Revs 0–6 used by A06 (26 effective crossings), we estimated P_{SW} values at each crossing from the pressure balance condition between magnetic and dynamic pressures used in that study (assuming a zero-beta magnetospheric plasma). The resulting relation between standoff distance (from the A06 geometry) and P_{SW} is shown in Figure 6. The best-fitting power law $R_{MP} \propto P_{SW}^{-1/\alpha_S}$ gave $\alpha_S = 5.17 \pm 0.30$, significantly higher than the original value obtained by A06 and indicative of a more rigid magnetosphere. Independently fitting the crossings for a compressed magnetosphere ($R_{MP} < 22\ R_S$) did not give a significantly different index. This value of α_S gives a value of P_{SW} approximately 50% smaller than the A06 value for the range $22 < R_{MP} < 27\ R_S$ (note that this change is of the order of the error in P_{SW} derived from the A06 model, see the following subsections and Figure 7).

[36] The data points for an expanded magnetosphere ($R_{MP} > 24\ R_S$) could not be used to constrain α_S (the error in the fitted α_S was of the order of the index itself). The addition of further magnetopause encounters to our database will enable us to pursue more detailed future studies of the possible influence of magnetospheric compression on α_S. This is particularly important for Saturn where observations of the outer magnetospheric field have shown that the noon sector can show transitions between "dipole-like"

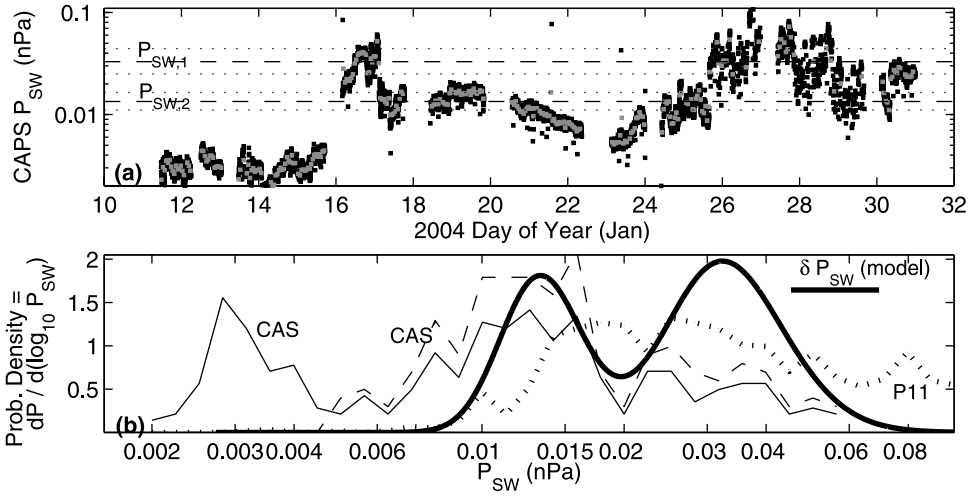

Figure 7. (a) The CAPS solar wind measurements used to derive the PDFs. Solar wind pressure on a log scale is shown as a function of time. The values of pressure corresponding to the best-fitting dual model are shown, using the same convention as for the top panel. The variable-resolution data are shown as black squares, and the 1-hour averaged data (see text) as gray squares. (b) Probability density functions for logarithm of solar wind pressure P_{SW}. Black heavy line is the prediction of the best-fitting dual model transformed to P_{SW} using the scaling law of A06 (see text) (the horizontal bar labeled δP_{SW} indicates the uncertainty of the estimated model pressure). The thin solid line shows the PDF calculated from 1 month of CAPS solar wind measurements (1-hour average), from 11 to 13 January 2004. The thin dashed line shows the CAPS PDF based on restricting the interval to 16 through 31 January 2004. The dotted curve shows the PDF derived from the Pioneer 11 solar wind data set for the period 19 July through 26 October 1979, which brackets the Saturn flyby (1 September) and covers about four solar rotations.

and "disk-like" field depending on the degree of compression [*Arridge et al.*, 2008]. This variability may be the reason why the Cassini studies, based on multiple spacecraft orbits and magnetospheric configurations, have produced compressibility indices α_S significantly smaller than the original study by *Slavin et al.* [1985], based on a few flybys of the planet. Variability in magnetospheric plasma beta and global mass, as well as departures from dynamic balance at the magnetopause, will contribute to the scatter of the points in Figure 6. We now consider some possible physical reasons for the bimodal distribution in Saturn's magnetopause size.

4.1. Solar Wind Variability

[37] J02 examined extensive solar wind data sets from spacecraft near Jupiter orbit and showed that the time-dependent behavior of dynamic pressure P_{SW} was one of the principal causes of the corresponding range in jovian magnetopause size. They observed a high-pressure (average ~0.2 nPa) solar wind about 40 percent of the time, with lower pressures (~0.047 nPa) otherwise. More recently, *Jackman et al.* [2004] have examined Cassini magnetometer data in the solar wind near Saturn, during the spacecraft's first approach to the planet. Using the IMF as an approximate indicator of compressions and rarefactions in the solar wind, they concluded that the interplanetary medium was in a compressed (high P_{SW} state) around ~20% of the time and in a state of lower P_{SW} otherwise (we further discuss analogous results with respect to our model and Cassini plasma data in section 4.2). The lack of extensive intervals of favorable spacecraft orientation prevented continuous measurements by the Cassini plasma spectrometer (CAPS) of P_{SW} which would have been nearly coincident with the intervals studied by *Jackman et al.* [2004] and in this paper. However, *Jackman et al.* [2004] pointed out that the dual states of the IMF were associated with the declining phase of the solar cycle, with usually two compression regions (with embedded crossings of the heliospheric current sheet) observed during each solar rotation. While the exact level of P_{SW} may thus vary between solar rotations, we would expect the recurrence of this pattern to produce a long-term pressure distribution with a time-dependent behavior showing compressed and rarified states, having distinct mean values of dynamic pressure (as shown by J02 near Jupiter).

[38] Panel (a) of Figure 7 shows a set of direct measurements of P_{SW} by the CAPS instrument during January 2004—while Cassini was ~0.23 AU upstream of Saturn. This is the same solar wind data used in the study by *Badman et al.* [2005] which examined the effect of solar wind compressions on the morphology of Saturn's aurora. The original data were taken with a range of time resolutions from ~16 s to ~6 min. These are shown as black squares. The gray squares show the data averaged in boxcar fashion (sample-and-hold interpolation) over adjacent 1-hour windows. Within each window, we required that, to be included in the averaged data, the original points had to be separated by <15 minutes from their nearest neighbors and that the difference in time between first and last points was >40 minutes.

[39] Panel (b) of Figure 7 compares the PDF associated with the dual model of best fit for R_{MP} and the PDF derived from the 1-hour CAPS averages for the time intervals 11–31 January and 16–31 January, labeled "CAS" (we further discuss this averaging interval later in this section). For comparison, we also show a PDF labeled "P11", derived from 1-hour averaged solar wind data from the

Pioneer 11 spacecraft, during an interval of four solar rotations encompassing the P11 Saturn encounter (see the figure caption). These data were downloaded from the Coordinated Heliospheric Observations database at the National Space Data Center (COHOweb). The PDFs have been plotted on a logarithmic pressure scale in order to accentuate features at higher values of P_{SW}, which varies over one and a half orders of magnitude. The horizontal bar labeled "δP_{SW}" indicates the ~40% relative error in pressure estimates arising from the uncertainties in the A06 model parameters. We see that in the region $0.009 < P_{SW} < 0.06$ nPa, both model and observed PDFs exceed values of a few percent. In this same region, there is a good agreement between the modeled and observed Cassini PDFs with respect to the height of the expanded component with a local maximum near 0.013 nPa—although the model prediction is somewhat narrower than the observations. The Pioneer 11 PDF corresponds to a time of high solar activity and extends to generally higher values of P_{SW} values than its Cassini counterparts.

[40] The compressed component in the model Cassini PDF which peaks at a higher P_{SW} near 0.035 nPa does not have a corresponding match with the plasma data. The observations do show a high-pressure tail in the PDF. However this component is associated with maximum probability densities which are approximately equal to half of the local maximum in the model's high-pressure component. The observed PDF therefore does not show evidence for the bimodality present in the model over the pressure range $0.005 < P_{SW} < 0.1$ nPa; a similar result was reported for Jupiter by J02. We note that there is an additional component in the observed PDF if we include data earlier than 16 January when the solar wind was at its lowest dynamic pressure during the interval of measurement. However, the low dynamic pressure indicated (0.003 nPa) is a factor ~5 less than the pressure at the "peak" for the expanded component of the model distribution (~0.014 nPa)—well beyond the estimated relative uncertainty in model P_{SW}. In other words, while we see a distinct additional peak at ~0.003 nPa in the observations earlier than 16 January, we do not identify it with either of the two distinct peaks required by the model in the range $0.005 < P_{SW} < 0.1$ nPa.

[41] Of course the CAPS measurements from January 2004 are not coincident with the magnetospheric spacecraft orbits we have studied, the first of which commenced about six months later. However, it is of interest to note that the separation between the two components of our dual model do agree reasonably well with the overall range of pressures observed by CAPS after 16 January in the compressed and rarefied regions of the solar wind. The higher-pressure regime is of interest because the observations indicate that here the mean pressure is elevated, while the short-term fluctuations in the compressed state, even in the 1-hour averages, are of the order of the difference in the average values between the compressed and expanded states. Such large fluctuations are not seen in the quieter rarefaction regions. This distinction is emphasized by the logarithmic scaling in the lower panel of Figure 7 and was also noted by *Jackman et al.* [2004] for the IMF. These large fluctuations are one reason why the observed PDF does not show the clear bimodality associated with the model. J02 pointed out the strong variability in the values of solar wind pressure at Jupiter orbit from one solar rotation to the next, applicable to both "high-pressure" and "low-pressure" time intervals. This is another factor which contributes to observed PDFs which are not bimodal, despite the time-dependent pattern of alternating compressions and rarefactions in the solar wind.

[42] This type of solar wind structure is the subject of a recent observational study by *Jackman et al.* [2008], which discusses how the solar wind evolves out to regions near Saturn orbit, ~9 AU from the Sun. It has been shown in this study, using ACE data at Earth, that the solar wind can be structured by compressions and rarefactions associated with Corotating Interaction Regions (CIRs). Analysis at Saturn shows that, particularly during the declining phase of the solar cycle, streams observed at Earth can steepen considerably at larger heliocentric distances [see also *Jackman et al.*, 2004]. In some cases, merging of CIRs to form Merged Interaction Regions (MIRs) can also occur, as the faster streams push the slower ones ahead of them.

4.2. Mass Loading and Rotational Anomaly

[43] We now consider internal mechanisms at Saturn which may contribute to the PDF of magnetopause standoff distance R_{MP}—in particular the bimodal nature of this function, as revealed by the distribution of Cassini magnetopause crossings. An important property of any internal physical mechanism which produces such a distribution is that it must produce changes in the internal state of the magnetosphere on time scales which are comparable to or shorter than those of typical spacecraft orbits. Two well-known possibilities are the action of the rotational anomaly at Saturn; and the continual addition of plasma to the magnetosphere by Enceladus, the icy satellites and the rings, combined with rapid mass loss associated with the Vasyliūnas cycle.

[44] The magnetic field strength and direction in Saturn's outer magnetosphere have been observed to be modulated at periods close to the planet's nominal rotation period, in Voyager, Pioneer and Cassini data [*Espinosa and Dougherty*, 2000; *Espinosa et al.*, 2003; *Giampieri et al.*, 2006]. This behavior has been hypothesized to be the result of a rotating magnetic "anomaly" at Saturn which launches "fast-mode" waves into the surrounding magnetosphere that form a "spiral-like" pattern as they propagate outward because of the planet's rotation [*Espinosa et al.*, 2003; *Cowley et al.*, 2006]. *Clarke et al.* [2006] studied the signatures of this anomaly in Cassini magnetic and plasma data for Revs 16 and 17 (2005 DOY 281–302, 8–29 October) and detected magnetopause crossings consistent with an oscillation of the boundary at the planetary period and an amplitude of order ~1 R_S. It was estimated that a corresponding change of ~40% in internal plasma pressure was required to effect such a change. We did not detect quasi-periodic patterns for the magnetopause crossings in the orbits considered for this study; however, the effect of the rotational anomaly should always be present and contribute to the statistical properties of R_{MP} over long enough time periods. If the estimates of *Clarke et al.* [2006] are typical of its influence, then we would expect the anomaly to be more effective at contributing to the scatter or standard deviation in the individual components of the

bimodal R_{MP} distribution ($\sigma_1 \sim 1.5\ R_S$ and $\sigma_2 \sim 1.3\ R_S$), rather than to the relatively large separation $\sim 5\ R_S$ between the two mean values associated with these components ($\mu_1 \sim 22\ R_S$ and $\mu_2 \sim 27\ R_S$).

[45] We have previously referred to the rate of plasma mass loading of the order $\sim$500 – 2000 kg s^{-1} at Jupiter, principally because of the Io source (see section 1 and references). At Saturn, the internal sources for plasma mass loading include the icy moons, particularly Enceladus, and the E ring. The moon Titan also contributes to this plasma mass source. The kronian mass loading rate for the magnetospheric plasma is much lower than in the jovian system. One estimate derived from Cassini observations of flow deflection near Enceladus yields a relatively high $\sim$100 kg s^{-1} [*Tokar et al.*, 2006]. On the other hand, analysis of ion-cyclotron waves in the Cassini magnetometer data gives a lower limit for mass loading rate $<\sim$10 kg s^{-1} from the E ring [*Leisner et al.*, 2006]. Electrodynamic and chemical modeling of the Enceladus source give consistent estimates of $\sim$2 kg s^{-1} [*Khurana et al.*, 2007: modeling magnetic signature of the planet-moon current system] and $\sim$2 – 3 kg s^{-1} [*Burger et al.*, 2007: chemical modeling of water group ion-neutral interaction] respectively. For the case of Titan, Cassini observations by the RPWS Langmuir probe yield an estimate of 10^{25} ions s^{-1} escaping from Titan's ionosphere [*Wahlund et al.*, 2005]. MHD and hybrid models of the Titan-magnetosphere interaction predict escape fluxes in the range 2.6×10^{24} – 5.6×10^{25} ions s^{-1}, corresponding to $\sim$0.1–1.3 kg s^{-1} including the species N_2^+, CH_4^+ and H_2^+ [*Modolo et al.*, 2007; *Ma et al.*, 2006]. The evidence presented by all of these studies thus favors a plasma mass loading rate which is a factor of 50 – 100 smaller for Saturn's magnetosphere, when compared to the average for the jovian system.

[46] While variability in mass loading will contribute to changing magnetosphere size at fixed solar wind dynamic pressure, very rapid mass loss processes at Saturn would also effectively contribute to the bimodal appearance of the magnetopause standoff distance. *Vasyliūnas* [2008] has pointed out that it is more physically meaningful to compare scaled mass loading rates at Jupiter and Saturn rather than absolute numbers. He proposes a scaling factor for mass loading rate $S_{cr} \propto \mu^2\Omega/r_s^5$ which involves the relevant parameters of planetary magnetic moment μ, planetary angular velocity Ω and orbital radius r_s of the moon (source of plasma). This quantity is a critical rate for mass outflow which attains a kinetic energy density at distance r_s that is comparable to the energy density of the planetary magnetic field (this magnitude of outflow is thus capable of strongly distorting the field at the moon's location). This critical rate is about 60 times larger for Jupiter than for Saturn. As a result, the scaled mass loading rate is actually higher for Saturn than Jupiter by a factor of $\sim$6. This comparison suggests that mass loss processes operating at both planets are capable of removing similar fractions of the mass of the plasma disk. In the following discussions, we consider a relevant time scale associated with replenishment of plasma disk mass at both planets by their internal sources (moons).

[47] *Kronberg et al.* [2005] examined periodicities in Galileo magnetic and plasma data at Jupiter's magnetotail region. They showed that the apparent 2- to 3-day cycle of plasma mass loading and release (see section 1) at that planet could be understood in terms of the time scale required for recently "emptied" flux tubes to be re-filled with plasma to the point where they once more became unstable and shed plasmoids downtail. This time scale was estimated to be inversely proportional to the plasma mass loading rate due to Io. It is also of the same order of magnitude as the $\sim$1 day timescale required for the internal source (Io) to provide a plasma mass of the order of that usually contained in Jupiter's magnetodisc ($\sim 10^8$ kg, [*Russell et al.*, 1999]). The equivalent physical timescale at Saturn, whose magnetodisc mass is $\sim 10^6$ kg [*Arridge et al.*, 2007] would be of the order of magnitude, $\sim$1 – 10 days (for a range of 1 – 10 kg s^{-1} plasma sources).

[48] Relevant in this context are the Cassini RPWS radio observations reported by *Louarn et al.* [2007], who identified radio signatures at Saturn showing very similar time-dependent behavior to the quasi-periodic (2–3 days) jovian "energetic events" reported by Galileo [*Woch et al.*, 1998; *Krupp et al.*, 1998]. These events were those interpreted by *Kronberg et al.* [2005] as being due to plasma loading and release processes at Jupiter. The recurrence period of the analogous kronian radio emissions, seen near midnight local time and at radial distances >20 R_S, was $\sim$5 – 10 days. Individual intensifications observed by *Louarn et al.* [2007] lasted several hours—these would be signatures of rapid reconfiguration associated with mass loss from the outer plasma disk in this picture.

[49] In terms of the necessarily-limited comparison between observed and modeled PDFs for the solar wind that we have made, the orbits we have studied extend over timescales which are large compared to the aforementioned filling times and radio periods. It is therefore likely that any effects of internal mass loading and loss would be captured within our data set. More detailed modeling in future studies should aim to reveal whether these processes change the magnetodisc mass by large fractions on the observed short time scales. If this is the case, it would be compelling evidence that these processes are the internal driver which acts simultaneously with solar wind dynamic pressure, and which is the cause of the bimodal magnetopause size. Figure 7c can be used to estimate an upper limit to the degree of influence of the internal driver, equivalent to a change of $\sim$0.02 nPa in pressure, or $\sim 5\ R_S$ in standoff distance (the separation between the two peaks of the model distribution). In other words, a variation comparable to that seen in the solar wind pressure data. We also note that the magnetodisc stress balance modeled at Saturn by *Arridge et al.* [2007] suggested some degree of internal control in magnetodisc formation, but with solar wind variability as the primary factor determining its structure.

5. Discussion and Summary

[50] We have used established statistical techniques [J02] and a new empirical model for Saturn's magnetopause [A06] in order to study the long-term variations in the size of this boundary. Our data samples were produced by applying the model to regularly-sampled orbits of the early tour of the Cassini spacecraft. We computed the probability distribution for the standoff distance R_{MP} and found that it was best described by a dual or bimodal distribution, using normal populations to represent a compressed and an

expanded magnetospheric configuration. Statistical tests generally supported the better quality of fit for this model, at significance levels $>\sim$10%, compared to near-zero significance for the single model.

[51] A comparison with a sequence of direct measurements of the solar wind dynamic pressure by the CAPS instrument revealed that the bimodal model predicted a solar wind distribution with similar features in the low-pressure regime. At higher pressures, the observations showed a monotonically decreasing PDF, rather than the second peak shown by the model. Strong, rapid fluctuations in solar wind pressure observed in the compressed mode contribute to this property of the observed PDF. Analysis by J02 of solar wind conditions near Jupiter also indicate that solar wind pressure is not bimodal. Consideration of the properties of mass loading and the rotational anomaly at Saturn indicate that these processes are likely to play an additional role to the solar wind in determining the detailed distribution of R_{MP}.

[52] The rotational anomaly has been observed to change magnetopause location during particular Cassini orbits by distances of the order 1 R_S [*Clarke et al.*, 2006]. This length scale is characteristic of the "spread" in magnetopause standoff distance at either of the two bimodal "peaks" in our distribution, but not the $\sim$5 R_S separation between the peaks. We thus expect that the rotational anomaly alone cannot explain the bimodal behavior. Mass loading and release from the magnetodisc seems to be a more promising candidate for explaining the bimodal form of the R_{MP} distribution. This is because observational signatures associated with the process (such as particle data and radio observations) indicate that episodes of mass loss last for several hours and recur at Saturn on time scales of $\sim$5 – 10 days. Observations indicate plasma mass loading rates for Saturn's magnetosphere capable of replenishing magnetodisc mass on time scales of 1 – 10 days. It follows that the processes of mass loading and release at Saturn could conceivably lead to global changes in magnetospheric plasma content which are rapid, occurring on time scales very short compared to spacecraft orbits which we use to sample physical conditions. This aspect of rapid transitions between distinct magnetospheric mass profiles is required for explaining the bimodal size distribution of the magnetopauses of both Saturn and Jupiter. Future modeling and observations should provide a more certain assessment of this proposed mechanism.

Appendix A: Statistical Analysis of Model Fits

[53] In this section, we objectively compare the quality of the best-fitting dual and single models described in section 3. We do this by using two statistical tests employed by J02 for their study and one additional test appropriate for this work. All of these tests follow the common formalism of testing the null hypothesis that the cumulative probability distribution observed in the data is drawn from a particular underlying model: either the dual (bimodal) or the single normal distribution. Each test calculates a prescribed "deviation" D between the data and the model. In general each test provides a means of computing the probability P_{TEST} ($D > D_{OBS}$) that D would exceed the observed value D_{OBS} if the null hypothesis were true. The smaller the value of this probability, the more confident we can be that the null hypothesis is not valid and that our model should be rejected. The probability P_{TEST} is often referred to as the level of significance with which the null hypothesis (or the model fit) may be accepted, with higher values indicating a better fit. Equivalently, a measure of the level of confidence with which we may reject a model is given by $1 - P_{TEST}$ ($D > D_{OBS}$). Commonly-used confidence levels for determining whether to reject a model are usually $\sim$90% or higher.

[54] We used three tests in this study, two used by J02 and a reduced chi-squared technique which specifically uses the estimated errors in the cumulative probability distribution and therefore provides a useful means of validating the other test results. These specific tests were the following:

[55] 1. Kolmogorov–Smirnov (KS) Test. The measured deviation D_{KS} is the maximum absolute value of the differences between the cumulative probability distributions of the data and the fitted model (see Figure 3a). This may be written:

$$D_{KS} = \max\left[P\left(R_{MP} > r_{MP}^{j}\right) - P_C\left(r_{MP}^{j}\right), j = 1..N\right] \tag{A1}$$

using the previous nomenclature (section 2, equation (3)). The number of data samples used in calculating the cumulative probabilities is also a required input for the KS test. For this number we used the number of samples in the bin whose computed probability showed the largest deviation from the model (i.e., the bin associated with D_{KS}).

[56] 2. Reduced "chi-squared" (χ_R^2) Test. The measured deviation D_{RCS} is given by a weighted sum of the squared differences between the observed and modeled cumulative probabilities. The inverse square of the error $s(r_{MP}^{j})$ in the cumulative probability was used as a weight for computing the measured deviation (see section 3).

$$D_{RCS} = \sum_{j=1}^{N} \left[\left(P\left(R_{MP} > r_{MP}^{j}\right) - P_C\left(r_{MP}^{j}\right)\right) / s\left(r_{MP}^{j}\right)\right]^2 \tag{A2}$$

[57] A reasonably good model fit would pass within $s(r_{MP}^{j})$ of the computed probability at each bin center, giving $D_{RCS} <\sim N$.

[58] 3. F Test. This test does not measure the difference between data and model but between two sets of measurements to test the null hypothesis that they are drawn from the same underlying population. Following J02, we apply the F test to two sets of differences: the first being the deviations between the estimated cumulative probability distribution and the best-fitting dual model; and the second being the deviations between the same data and the best-fitting single model. The parameter required for the F test is the ratio of the variance in the residuals associated with the single and dual model fits:

$$\begin{aligned}\xi_F &= v_{SNGL}/v_{DUAL} \\ &= \left[\sum_{j=1}^{N}\left(P\left(R_{MP} > r_{MP}^{j}\right) - P_{C,SNGL}\left(r_{MP}^{j}\right)\right)^2/(N - m_{SNGL})\right] \\ &\quad \Big/ \left[\sum_{j=1}^{N}\left(P\left(R_{MP} > r_{MP}^{j}\right) - P_{C,DUAL}\left(r_{MP}^{j}\right)\right)^2/(N - m_{DUAL})\right]\end{aligned} \tag{A3}$$

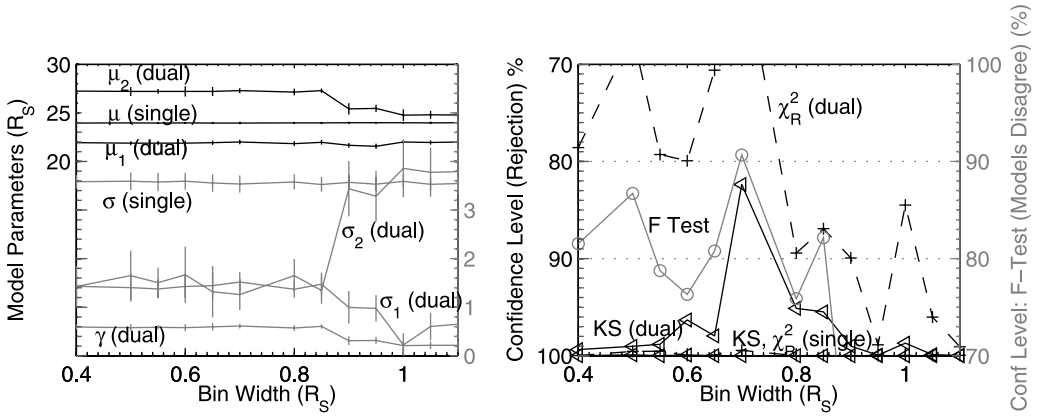

Figure A1. Results of statistical tests for quality of fit associated with the single and dual population models for magnetopause standoff distance (see text). The left panel shows the fitted model parameters and their estimated errors as a function of bin size. The right panel shows confidence levels for model comparison/rejection, as a function of bin size, for the F test (gray line, open circles), Kolmogorov–Smirnov (KS) test (dashed lines, triangles) and the Reduced Chi-Squared (χ^2_R) test (solid black lines, crosses). For both panels, black and gray points and curves correspond to vertical axes of the same color.

[59] We found that the variance for the single fit was always larger than for the dual fit. The definition of ξ_F also contains the number of model parameters, which for the single model is $m_{\mathrm{SNGL}} = 2$ and for the dual $m_{\mathrm{DUAL}} = 5$ (equation (3)). The difference between the number of bin centers N and the number of model parameters m represents the degrees of freedom associated with the test.

[60] We show in Figure A1 (left panel) the variation of the fitted model parameters as a function of bin size. We see that, for bin sizes $<\sim 0.8\ R_S$, they remain stable and change very little compared to their estimated uncertainties. Beyond this limit, the dual model parameters are not as well-constrained by the coarser binning and show larger relative "point-to-point" variations.

[61] We also show in Figure A1 (right panel) the results of the three statistical tests as a function of the bin size Δr_{MP}. For the F test, we show the level of confidence with which we may reject the null hypothesis that the model residuals are statistically equivalent (from the same population). For the other tests, we show the level of confidence with which we may reject a model as a description of the true distribution from which our samples r_{MP} (t_i) were drawn. If we firstly consider the results for the F test, we see that for bin sizes near 0.5 and 0.7 R_S we may, at a confidence level >85%, reject the hypothesis that the two models give equivalent residuals. In other words, we can accept that the dual model provides a better fit (smaller residuals) at this level of significance. For larger bin sizes, the coarser resolution in r_{MP} produces smaller differences in the residuals for the two fitted models and we can no longer reject their equivalence with confidence >85%.

[62] For bin sizes 0.65 – 0.75 R_S the K-S test indicates that the dual model cannot be rejected with $>\sim$90% confidence. The general trend of the χ^2_R test shows a dual model fit of equal or better quality for bin widths $<\sim 0.9\ R_S$ (for this range, the dual model cannot be rejected at confidences ranging between $\sim$50% and $\sim$90%). Like the KS test, it generally shows a poorer quality of fit with increasing bin size. The most remarkable feature of Figure A1 is that the tests indicate a consistent near-100% level of confidence (within a few percent) for rejection of the single model fit, regardless of bin size. This is in marked contrast to the results described for the dual model. Taken as a whole, the statistical results support the dual model being a better description of the data at the levels of significance indicated in Figure A1.

[63] **Acknowledgments.** NA acknowledges the support of a PPARC research fellowship while at Imperial College and useful discussions with R. J. Walker. CSA acknowledges the support of a PPARC quota studentship at Imperial College and the STFC rolling grant to MSSL/UCL. We acknowledge the support of the MAG data processing/distribution staff at Imperial College, JPL and UCLA: S. Kellock, P. Slootweg, T. Seears, J. Wolfe and L. Lee. We also acknowledge useful discussions with F. Crary regarding the Cassini CAPS data set.

[64] Wolfgang Baumjohann thanks Vytenis Vasyliunas and another reviewer for their assistance in evaluating this paper.

References

Achilleos, N., et al. (2006), Orientation, location, and velocity of Saturn's bow shock: Initial results from the Cassini spacecraft, *J. Geophys. Res.*, *111*, A03201, doi:10.1029/2005JA011297.

Achilleos, N., C. S. Arridge, H. J. McAndrews, A. Masters, M. K. Dougherty, and A. J. Coates (2007), High-latitude structure of Saturn's magnetopause: Cassini observations, *Eos Trans. AGU*, *88*(52), *Fall Meet. Suppl.*, Abstract P53D-01.

Arridge, C. S., N. Achilleos, M. K. Dougherty, K. K. Khurana, and C. T. Russell (2006), Modeling the size and shape of Saturn's magnetopause with variable dynamic pressure, *J. Geophys. Res.*, *111*, A11227, doi:10.1029/2005JA011574.

Arridge, C. S., C. T. Russell, K. K. Khurana, N. Achilleos, N. André, A. M. Rymer, M. K. Dougherty, and A. J. Coates (2007), Mass of Saturn's magnetodisc: Cassini observations, *Geophys. Res. Lett.*, *34*, L09108, doi:10.1029/2006GL028921.

Arridge, C. S., C. T. Russell, K. K. Khurana, N. Achilleos, S. W. H. Cowley, M. K. Dougherty, D. J. Southwood, and E. J. Bunce (2008), Saturn's magnetodisc current sheet, *J. Geophys. Res.*, *113*, A04214, doi:10.1029/2007JA012540.

Acuña, M. H., K. W. Behannon, and J. E. P. Connerney (1983), Jupiter's magnetic field and magnetosphere, in *Physics of the Jovian Magnetosphere*, edited by A. J. Dessler, pp. 1–50, Cambridge Univ. Press, Cambridge.

Badman, S. V., E. J. Bunce, J. T. Clarke, S. W. H. Cowley, J.-C. Gérard, D. Grodent, and S. E. Milan (2005), Open flux estimates in Saturn's magnetosphere during the January 2004 Cassini-HST campaign, and implications for reconnection rates, *J. Geophys. Res.*, *110*, A11216, doi:10.1029/2005JA011240.

Bagenal, F. (1997), Ionization source near Io from Galileo wake data, *Geophys. Res. Lett.*, *24*, 2111–2114.
Behannon, K. W., R. P. Lepping, and N. F. Ness (1983), Structure and dynamics of Saturn's outer magnetosphere and boundary regions, *J. Geophys. Res.*, *88*, 8791–8800.
Burger, M. H., E. C. Sittler, R. E. Johnson, H. T. Smith, O. J. Tucker, and V. I. Shematovich (2007), Understanding the escape of water from Enceladus, *J. Geophys. Res.*, *112*, A06219, doi:10.1029/2006JA012086.
Clarke, K. E., et al. (2006), Cassini observations of planetary-period oscillations of Saturn's magnetopause, *Geophys. Res. Lett.*, *33*, L23104, doi:10.1029/2006GL027821.
Coleman, T. F., and Y. Li (1996), An interior, trust region approach for nonlinear minimization subject to bounds, *SIAM J. Optim.*, *6*, 418–445.
Cowley, S. W. H., D. M. Wright, E. J. Bunce, A. C. Carter, M. K. Dougherty, G. Giampieri, J. D. Nichols, and T. R. Robinson (2006), Cassini observations of planetary-period magnetic field oscillations in Saturn's magnetosphere: Doppler shifts and phase motion, *Geophys. Res. Lett.*, *33*, L07104, doi:10.1029/2005GL025522.
Crary, F. C., et al. (2005), Solar wind dynamic pressure and electric field as the main factors controlling Saturn's aurorae, *Nature*, *433*, 720–722.
Delamere, P. A., and F. Bagenal (2003), Modeling variability of plasma conditions in the Io torus, *J. Geophys. Res.*, *108*(A7), 1276, doi:10.1029/2002JA009706.
Espinosa, S. A., and M. K. Dougherty (2000), Periodic perturbations in Saturn's magnetic field, *Geophys. Res. Lett.*, *27*, 2785–2788.
Espinosa, S. A., D. J. Southwood, and M. K. Dougherty (2003), How can Saturn impose its rotation period in a noncorotating magnetosphere?, *J. Geophys. Res.*, *108*(A2), 1086, doi:10.1029/2001JA005084.
Giampieri, G., M. K. Dougherty, E. J. Smith, and C. T. Russell (2006), A regular period for Saturn's magnetic field that may track its internal rotation, *Nature*, *441*, 62–64.
Hill, T. W. (1980), Corotation lag in Jupiter's magnetosphere—Comparison of observation and theory, *Science*, *207*, 301–302.
Hill, T. W., A. J. Dessler, and F. C. Michel (1974), Configuration of the Jovian magnetosphere, *Geophys. Res. Lett.*, *1*, 3–6.
Huddleston, D. E., C. T. Russell, M. G. Kivelson, K. K. Khurana, and L. Bennett (1998), Location and shape of the Jovian magnetopause and bow shock, *J. Geophys. Res.*, *103*, 20,075–20,082.
Jackman, C. M., N. Achilleos, E. J. Bunce, S. W. H. Cowley, M. K. Dougherty, G. H. Jones, S. E. Milan, and E. J. Smith (2004), Interplanetary magnetic field at ~9 AU during the declining phase of the solar cycle and its implications for Saturn's magnetospheric dynamics, *J. Geophys. Res.*, *109*, A11203, doi:10.1029/2004JA010614.
Jackman, C. M., R. J. Forsyth, and M. K. Dougherty (2008), The overall configuration of the interplanetary magnetic field upstream of Saturn as revealed by Cassini observations, *J. Geophys. Res.*, *113*, A08114, doi:10.1029/2008JA013083.
Joy, S. P., M. G. Kivelson, R. J. Walker, K. K. Khurana, C. T. Russell, and T. Ogino (2002), Probabilistic models of the Jovian magnetopause and bow shock, *J. Geophys. Res.*, *107*(A10), 1309, doi:10.1029/2001JA009146.
Khurana, K. K., M. K. Dougherty, C. T. Russell, and J. S. Leisner (2007), Mass loading of Saturn's magnetosphere near Enceladus, *J. Geophys. Res.*, *112*, A08203, doi:10.1029/2006JA012110.
Khurana, K. K., and M. G. Kivelson (1993), Inference of the angular velocity of plasma in the Jovian magnetosphere from the sweepback of magnetic field, *J. Geophys. Res.*, *98*, 67–79.
Kivelson, M. G., et al. (1997), Galileo at Jupiter—Changing states of the magnetosphere and first looks at Io and Ganymede, *Adv. Space Res.*, *20*, 193–204.
Kivelson, M. G., and D. J. Southwood (2005), Dynamical consequences of two modes of centrifugal instability in Jupiter's outer magnetosphere, *J. Geophys. Res.*, *110*, A12209, doi:10.1029/2005JA011176.
Kronberg, E. A., J. Woch, N. Krupp, A. Lagg, K. K. Khurana, and K.-H. Glassmeier (2005), Mass release at Jupiter: Substorm-like processes in the jovian magnetotail, *J. Geophys. Res.*, *110*, A03211, doi:10.1029/2004JA010777.
Krupp, N., J. Woch, A. Lagg, B. Wilken, S. Livi, and D. J. Williams (1998), Energetic particle bursts in the predawn Jovian magnetotail, *Geophys. Res. Lett.*, *25*, 1249–1252.
Leisner, J. S., C. T. Russell, M. K. Dougherty, X. Blanco-Cano, R. J. Strangeway, and C. Bertucci (2006), Ion cyclotron waves in Saturn's E-ring: Initial Cassini observations, *Geophys. Res. Lett.*, *33*, L11101, doi:10.1029/2005GL024875.
Louarn, P., et al. (2007), Observations of similar radio signatures at Saturn and Jupiter: Implications for the magnetospheric dynamics, *Geophys. Res. Lett.*, *34*, L20113, doi:10.1029/2007GL030368.
McAndrews, H. J., C. J. Owen, M. F. Thomsen, B. Lavraud, A. J. Coates, M. K. Dougherty, and D. T. Young (2008), Evidence for reconnection at Saturn's magnetopause, *J. Geophys. Res.*, *113*, A04210, doi:10.1029/2007JA012581.
Ma, Y., A. F. Nagy, T. E. Cravens, I. V. Sokolov, K. C. Hansen, J.-E. Wahlund, F. J. Crary, A. J. Coates, and M. K. Dougherty (2006), Comparisons between MHD model calculations and observations of Cassini flybys of Titan, *J. Geophys. Res.*, *111*, A05207, doi:10.1029/2005JA011481.
Modolo, R., G. M. Chanteur, J.-E. Wahlund, P. Canu, W. S. Kurth, D. Gurnett, A. P. Matthews, and C. Bertucci (2007), Plasma environment in the wake of Titan from hybrid simulation: A case study, *Geophys. Res. Lett.*, *34*, L24S07, doi:10.1029/2007GL030489.
Petrinec, S. M., and C. T. Russell (1997), Hydrodynamic and MHD equations across the bow shock and along the surfaces of planetary obstacles, *Space Sci. Rev.*, *79*, 757–791.
Russell, C. T. (1985), Planetary bow shocks, in *Collisionless Shocks in the Heliosphere: Reviews of Current Research, AGU Monogr. Ser.*, *35*, edited by R. G. Stone and B. T. Tsurutani, 109–130.
Russell, C. T., D. E. Huddleston, K. K. Khurana, and M. G. Kivelson (1999), Structure of the Jovian magnetodisk current sheet: Initial Galileo observations, *Planet. Space Sci.*, *47*, 1101–1109.
Russell, C. T., K. K. Khurana, M. G. Kivelson, and D. E. Huddleston (2000), Substorms at Jupiter: Galileo observations of transient reconnection in the near tail, *Adv. Space Res.*, *26*, 1499–1504.
Scarf, F. L., W. S. Kurth, D. A. Gurnett, H. S. Bridge, and J. D. Sullivan (1981), Jupiter tail phenomena upstream from Saturn, *Nature*, *292*, 585–586.
Shue, J. H., J. K. Chao, H. C. Fu, C. T. Russell, P. Song, K. K. Khurana, and H. J. Singer (1997), A new functional form to study the solar wind control of the magnetopause size and shape, *J. Geophys. Res.*, *102*, 9497–9511.
Slavin, J. A., E. J. Smith, J. R. Spreiter, and S. S. Stahara (1985), Solar wind flow about the outer planets: Gas dynamic modeling of the Jupiter and Saturn bow shocks, *J. Geophys. Res.*, *90*, 6275–6286.
Spreiter, J. R., A. L. Summers, and A. Y. Alksne (1966), Hydromagnetic flow around the magnetosphere, *Planet. Space Sci.*, *14*, 223–250.
Stahara, S. S., R. R. Rachiele, J. R. Spreiter, and J. A. Slavin (1989), A three dimensional gasdynamic model for solar wind flow past nonaxisymmetric magnetospheres: Application to Jupiter and Saturn, *J. Geophys. Res.*, *94*, 13,353–13,365.
Tokar, R. L., et al. (2006), The interaction of the atmosphere of Enceladus with Saturn's plasma, *Science*, *311*, 1409–1412.
Vasyliūnas, V. M. (1983), Plasma distribution and flow, in *Physics of the Jovian Magnetosphere*, edited by A. J. Dessler, pp. 395–453, Cambridge Univ. Press, Cambridge.
Vasyliūnas, V. M. (2008), Comparing Jupiter and Saturn: Dimensionless input rates from plasma sources within the magnetosphere, *Ann. Geophys.*, *26*, 1341–1343.
Wahlund, J.-E., et al. (2005), Cassini measurements of cold plasma in the ionosphere of Titan, *Science*, *308*, 986–989.
Walker, R. J., and C. T. Russell (1995), Solar wind interactions with magnetized planets, in *Introduction to Space Physics*, edited by M. G. Kivelson and C. T. Russell, pp. 129–163, Cambridge Univ. Press, Cambridge.
Woch, J., N. Krupp, A. Lagg, B. Wilken, S. Livi, and D. J. Williams (1998), Quasi-periodic modulations of the Jovian magnetotail, *Geophys. Res. Lett.*, *25*(8), 1253–1256.

N. Achilleos, Atmospheric Physics Laboratory, University College London, Gower Street, London WC1E 6BT, UK. (nick@apl.ucl.ac.uk)
C. S. Arridge, Mullard Space Science Laboratory / Centre for Planetary Sciences, University College London, Holmbury St. Mary, Dorking, Surrey, RH5 6NT, UK. (csa@mssl.ucl.ac.uk)
C. Bertucci, Institute for Astronomy and Space Physics (IAFE), P.O. Box 67, Suc. 28, C1428AA Buenos Aires, Argentina.
M. K. Dougherty and C. M. Jackman, Space and Atmospheric Physics Group, Blackett Laboratory, Imperial College London, Prince Consort Road London SW7 2BW, UK. (m.dougherty@imperial.ac.uk; c.jackman@imperial.ac.uk)
K. K. Khurana and C. T. Russell, Institute of Geophysics and Planetary Physics, University of California – Los Angeles, 3845 Slichter Hall, 603 Charles E. Young Drive, East Los Angeles, CA 90095-1567, USA. (kkhurana@igpp.ucla.edu)